

## Self-contained dual-scale composite architectures in spray dried zirconium diboride

Makurunje, Phylis; Woodhouse, Guy; Goddard, Dave; Middleburgh, Simon

### Ceramics International

DOI:

[10.1016/j.ceramint.2022.03.018](https://doi.org/10.1016/j.ceramint.2022.03.018)

Published: 15/06/2022

Peer reviewed version

[Cyswllt i'r cyhoeddiad / Link to publication](#)

*Dyfyniad o'r fersiwn a gyhoeddwyd / Citation for published version (APA):*

Makurunje, P., Woodhouse, G., Goddard, D., & Middleburgh, S. (2022). Self-contained dual-scale composite architectures in spray dried zirconium diboride. *Ceramics International*, 48(12), 17529-17538. <https://doi.org/10.1016/j.ceramint.2022.03.018>

### Hawliau Cyffredinol / General rights

Copyright and moral rights for the publications made accessible in the public portal are retained by the authors and/or other copyright owners and it is a condition of accessing publications that users recognise and abide by the legal requirements associated with these rights.

- Users may download and print one copy of any publication from the public portal for the purpose of private study or research.
- You may not further distribute the material or use it for any profit-making activity or commercial gain
- You may freely distribute the URL identifying the publication in the public portal ?

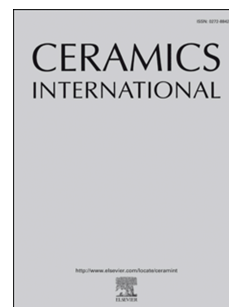
### Take down policy

If you believe that this document breaches copyright please contact us providing details, and we will remove access to the work immediately and investigate your claim.

# Journal Pre-proof

Self-contained dual-scale composite architectures in spray dried zirconium diboride

Phylis Makurunje, Guy Woodhouse, Dave T. Goddard, Simon C. Middleburgh



PII: S0272-8842(22)00755-6

DOI: <https://doi.org/10.1016/j.ceramint.2022.03.018>

Reference: CERI 31949

To appear in: *Ceramics International*

Received Date: 16 December 2021

Revised Date: 1 March 2022

Accepted Date: 2 March 2022

Please cite this article as: P. Makurunje, G. Woodhouse, D.T. Goddard, S.C. Middleburgh, Self-contained dual-scale composite architectures in spray dried zirconium diboride, *Ceramics International* (2022), doi: <https://doi.org/10.1016/j.ceramint.2022.03.018>.

This is a PDF file of an article that has undergone enhancements after acceptance, such as the addition of a cover page and metadata, and formatting for readability, but it is not yet the definitive version of record. This version will undergo additional copyediting, typesetting and review before it is published in its final form, but we are providing this version to give early visibility of the article. Please note that, during the production process, errors may be discovered which could affect the content, and all legal disclaimers that apply to the journal pertain.

© 2022 Published by Elsevier Ltd.

## Self-contained dual-scale composite architectures in spray dried zirconium diboride

Phylis Makurunje<sup>1\*</sup>, Guy Woodhouse<sup>2</sup>, Dave T. Goddard<sup>2</sup> and Simon C. Middleburgh<sup>1</sup>

<sup>1</sup> Nuclear Futures Institute, Bangor University, Bangor, Gwynedd, LL57 1UT, United Kingdom

<sup>2</sup> National Nuclear Laboratory, Preston Laboratory, Springfields, Preston, Lancashire PR4 0XJ, United Kingdom

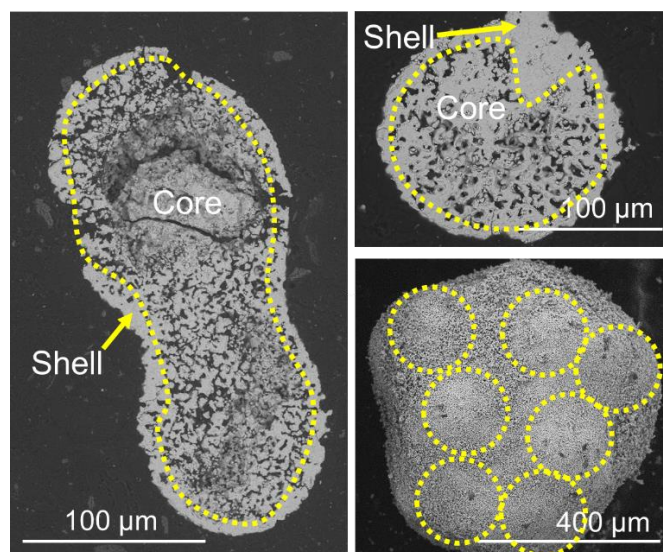
\*Corresponding author:

E-mail: [p.makurunje@bangor.ac.uk](mailto:p.makurunje@bangor.ac.uk) Tel: +44 1248 388 679

### Abstract

Zirconium diboride microspheres are candidate nuclear fuel additives. Dual-scale composite architectures (DCA) were produced in spray dried and sintered zirconium diboride microspheres. These findings expand the conventionally accepted hollow (“shell”), partially hollow (“dimpled”) and shrivelled (“wrinkled”) architectures previously reported in literature. Three-dimensional architectures of internally and externally detailed features on the microscale have been characterised by scanning electron microscopy. Core-shell architectures reported have maximum Feret diameters between  $216.4 \pm 58.7 \mu\text{m}$  and  $450.7 \pm 79.9 \mu\text{m}$ , while clustered granulate architectures have maximum Feret diameters of  $830.0 \pm 86.4 \mu\text{m}$ . Calculated dimensionless Peclet, Weber and Ohnesorge numbers of 0.16-0.21, 28.3, and 0.6-1.3 were obtained, respectively, and related to the morphologies of the microspheres obtained. Not only does this study show that the resultant architecture can be obtained, but also that the spray dried granulate morphologies are dependent on the binder quantity used. Microsphere architectures have potential utility in the accommodation of fission products expected during reactor operation.

### Graphical Abstract



## 1 Introduction

A candidate composite nuclear fuel concept consists of fissile ceramic microspheres dispersed in a fissile matrix, to boost thermophysical and thermochemical fuel stability during normal operation and in the event of anticipated operational occurrences (AOOs) or design-basis accidents [1], [2]. Ceramic materials like uranium diboride ( $\text{UB}_2$ ) [3], uranium silicide ( $\text{U}_3\text{Si}_2$ ) [4] and uranium nitride (UN) [5], [6] are embedded in the parent nuclear fuel, typically uranium oxide ( $\text{UO}_2$ ). However, non-fissile ceramics, such as zirconium diboride ( $\text{ZrB}_2$ ) are also potential microsphere materials for accident tolerant composite fuels. In the case of composite nuclear fuels design, such microspheres are typically made from ceramics of higher thermal conductivity than the fissile uranium oxide matrix [7], [8] as this will reduce centreline temperatures and associated adverse behaviours.

Zirconium diboride is a promising candidate ceramic microsphere material as it has a thermal conductivity of  $127 \text{ W}/(\text{m}\cdot\text{K})$  [7] compared to uranium dioxide's  $20 \text{ W}/(\text{m}\cdot\text{K})$  [8] at  $25^\circ\text{C}$ , and  $80 \text{ W}/(\text{m}\cdot\text{K})$  [7] compared to  $\sim 2 \text{ W}/(\text{m}\cdot\text{K})$  [8] at  $2000^\circ\text{C}$  (unirradiated). Furthermore, zirconium diboride has a melting point above  $3000^\circ\text{C}$  [9], and has the best oxidation resistance of all transition metal borides at given oxygen partial pressures above  $1000^\circ\text{C}$  [10], [11]. Zirconium diboride's impressive high temperature mechanical robustness [12]–[14] earns its consideration in nuclear fuels and reactor components for structural integrity beyond  $2000^\circ\text{C}$ .

In addition to the thermophysical and thermochemical robustness of zirconium diboride, the absorption of thermal neutrons, by boron-10, which leads to the release of helium-4 ( $^4\text{He}$ ) and lithium-7 ( $^7\text{Li}$ ) products [15] is used to control the reactivity in fission fuels, hence the application of zirconium diboride coatings as integral fuel burnable absorbers in pressurised water reactors [16], [17]. Data on zirconium diboride's response to fusion irradiations is growing, for example  $\text{He}^+$  at  $30 \text{ keV}$  with fluences of up to  $5.0 \times 10^{22}$  have been studied for tokamak applications [18].

Spray drying, a particle engineering process, has found wide and established applications in pharmaceutical, food and ceramic industries. Spray drying involves the atomisation of a liquid stream into a chamber in which the formed droplets collide with a hot stream of air that effects moisture evaporation. The drying of the droplets results in microspheres. The application of this process to the manufacture of nuclear fuel microspheres, be it fissile or non-fissile, has received little attention. An example is the process at the Australian Atomic Energy Commission research unit at Lucas Heights in the 1970s. Experiments were conducted to consider spray drying as an alternative route to the 3-step process of filtration, belt drying and rotary drum granulation for a proposed plant for up to  $500 \text{ tonne/yr}$  uranium-basis [19]. Dissolution of ores in nitric acid for solvent extraction of the uranyl nitrate preceded precipitation by ammonia and vacuum filtration of the yellow cake produced [19]. Thus spray drying aimed at producing uniformly sized granulates of the yellow cake – ammonium diuranate (ADU) – residue [20].

One reason for the limited application of spray drying approaches is the narrow feasibility range of achieving a Peclet number below unit (described in Section 2) to obtain solid (non-hollow) spheres. Hollow “shell” and dimpled spheres are the usual morphologies of spray dried products [21], [22]. Otherwise, wrinkled irregular-shaped granulates are formed depending on the material and/or process parameters applied [21].

In the present study, zirconium diboride slurries were spray dried with the aim of realising solid (non-hollow) spherical granulates. The spray drying process was selected as a route that has had limited demonstrations in non-oxide ceramics, let alone nuclear fuel microspheres.  $\text{ZrB}_2$  microspheres with self-contained dual-scale composite architectures that would lead to an accident tolerant  $\text{ZrB}_2$ -reinforced- $\text{UO}_2$  fuel with channels for fission products containment were obtained and characterised. As sol-gel processing is the *de facto* method for realising nuclear fuel microspheres, the present work provides results for future comparison.

## 2 Theory of Spray Drying Regimes

The spray drying process is dependent on multiple phenomena of fluid flow, mass transfer and heat transfer [23]. The morphology of the spray dried granulates is determined by the dominating phenomena, expressed by various dimensionless number calculations characteristic of the fluid flow, mass transfer and heat transfer phenomena. Dimensionless numbers Peclet (fluid flow compared to mass transfer and/or heat transfer), Weber (fluid flow) and Ohnesorge (fluid flow) numbers are pertinent to the resultant morphology of spray dried granulates and are discussed in subsequent subsection.

### 2.1 Peclet, Weber and Ohnesorge Dimensionless Numbers

The Peclet number ( $Pe$ ) predicts the morphology of the granulates formed, whether hollow or solid. The Peclet number compares mass transfer by fluid flow to diffusion. Alternatively, it compares heat transfer by motion of a fluid to heat transfer by thermal conduction. In the present study we calculated the  $Pe$  value (Equation (1a)) by measured values of viscosity and shear on the slurry and relating it to the Boltzmann constant [23]. As an alternative, Equation (1b) can be used. The realisation of  $Pe < 1$  leads to solid architectures [24].

The atomisation of the slurry - the breakage of the slurry stream to droplets – is explained numerically by the Weber and Ohnesorge numbers. The Weber number ( $We$ ) is a dimensionless number that compares the atomising gas inertia and slurry surface tension (Equation (2)). The impact of the atomising gas on the cohesive force of the slurry describes regimes of how the slurry breaks up when forming droplets. The critical  $We$  is the threshold breakup point for droplet formation.

The Ohnesorge numbers ( $Oh$ ) considers the viscosity of the slurry and compares the viscous forces to the surface tension of the slurry (Equation (3)). On the other hand, the Reynolds number ( $Re$ ), the arguably commonest fluid flow dimensionless number, is related to the  $We$  and  $Oh$  by Equation (4). The  $Re$  relates the atomising gas impacting force on the viscous forces of the slurry.

As the  $We$  and  $Oh$  are dependent on the flow rates of both the atomising gas and the slurry, the gas-to-liquid ratio (GLR) becomes an important relationship to highlight (Equation (5)). Kaser [25] showed that the median spray droplet size is strongly dependent on the ratio of liquid-to-gas flow rates, both on a mass and on a volume basis. The inverse ratio, slurry to gas mass flow rate,  $\mu_m = \dot{m}_s/\dot{m}_g$  is sometimes used to highlight how droplet size is dependent on it [26]. The  $\mu_m$  term often shows the efficiency – conversion of the atomising energy to the creation of finer droplet surfaces [26].

$$Pe = 6\pi\mu_s\gamma R_d^3/k_B T_s \quad (1a)$$

$$Pe = \mu_s \rho_s C_p D_d / k_B \quad (1b)$$

$$We = \rho_g u^2 D_d / \sigma_s \quad (2)$$

$$Oh = \mu_s / (D_d p_s \sigma_s)^{0.5} \quad (3)$$

$$Re = We^{0.5} / Oh \quad (4)$$

$$GLR = \dot{m}_g / \dot{m}_s \quad (5)$$

Where  $\rho_g$  and  $\rho_s$  are atomising gas and slurry densities respectively,  $\mu_s$  is slurry viscosity,  $\gamma$  is shear force,  $u$  is atomising gas velocity,  $\sigma_s$  is surface tension,  $D_d$  is the nozzle diameter,  $R_d$  is the particle size in slurry,  $k_B$  the Boltzmann constant,  $T_s$  is the spraying inlet temperature,  $C_p$  the heat capacity of the slurry and  $\dot{m}_g$  and  $\dot{m}_s$  are atomising gas and slurry mass flow rates, respectively.

### 3 Materials and Experimental Procedure

#### 3.1 Preparation

Commercial  $ZrB_2$  powders (American Elements, Los Angeles, CA, United States) of nominal 5  $\mu m$  particle size and 99.8% purity were used in this study. The  $ZrB_2$  slurry was prepared by adding and stirring 3 drops of Dolapix CE64 (Zschimmer and Schwarz, Germany) a proprietary anethanolaminic salt of citric acid [27], 0.25 g of 6k and 0.25 g of 20k polyethylene glycol (PEG: Alfa Aesar, United Kingdom) into 25 ml of distilled water. 45 g of the  $ZrB_2$  powder was added gradually to the solution, with magnetic mixing at 400 rpm for 15 min. In the first experiment 0.25 g each of the 6k and 20k PEG were used to prepare the slurry which shall be referred to in short as S1, while in the second experiment 0.5 g each of the 6k and 20k PEG were used to prepare the slurry which shall be referred to as S2. As such, the total binder in S1 and S2 slurries was 2 and 4 wt%, respectively, of the zirconium powder used.

#### 3.2 Spray Drying and Sintering

A Yamato DL410 (Yamato Scientific, Tokyo, Japan) spray dryer was used in this study. The inlet air temperature was set to 250 °C and the  $ZrB_2$  slurries were spray dried when the temperatures stabilised at 190 °C (inlet) and 95 °C (outlet). Details of the nozzle are shown in Figure 2b-c, and the nominal nozzle orifice diameter for the slurry was 2.5 mm (Figure 2c right). The calculated slurry flowrate was 41.6 ml/min from the manufacturer's settings [28].



An air spray was used to blow away fines attached to the surface of the desired microspheres. The spheres were subsequently loaded onto a zirconia crucible and heat treated in air in a muffle furnace set at 1750 °C with a 10 °C/min ramp up and 4 h dwell time, before cooling down at 10 °C/min to 500 °C and natural cooling thereafter.

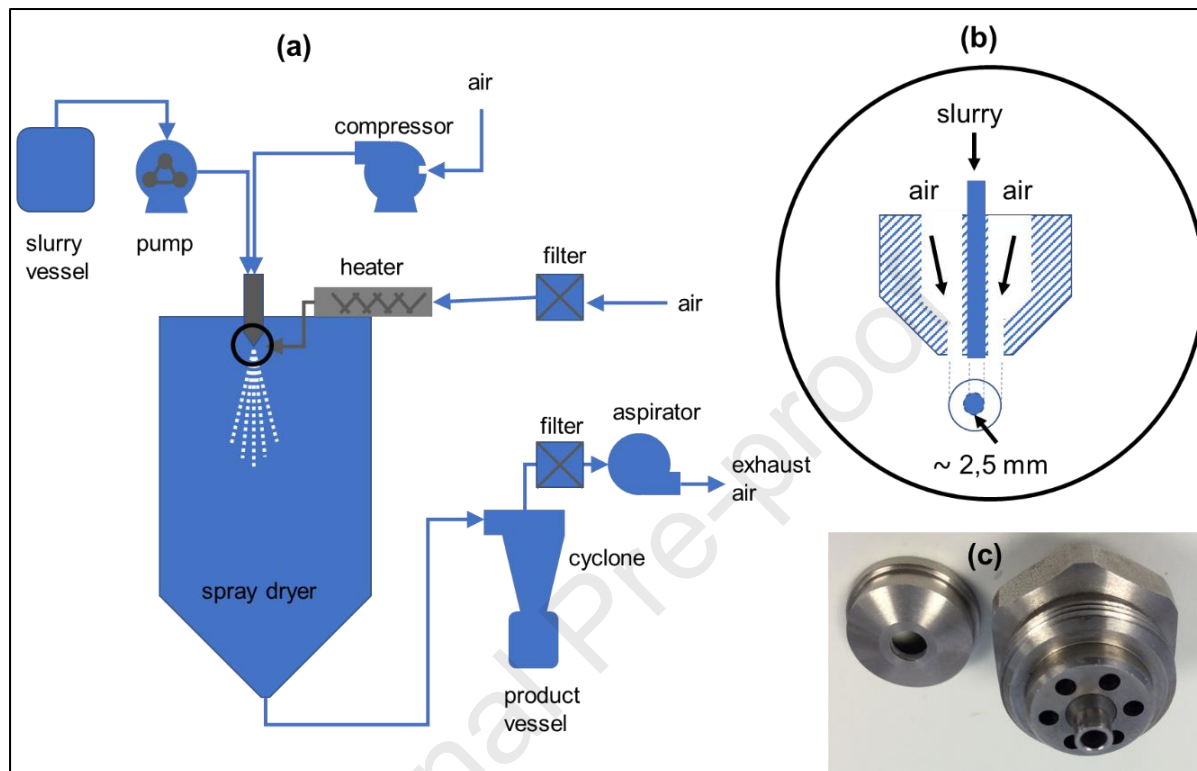


Figure 1: (a) The spray dryer system process flow diagram. The encircled region is the spraying nozzle. (b) An enlarged schematic of the air and slurry stream spraying nozzle encircled in (a). (c) Photograph of the gas cap (left) and the slurry cap (right) of the spraying nozzle.

### 3.3 Characterisation

The viscosities of the slurries were measured digitally (QC Visco300, Anton Paar GmbH, Graz, Austria) using the special small sample adapter CC26. The oxidation resistance of the  $\text{ZrB}_2$  during spray drying was investigated by comparing the X-ray diffraction (XRD; PANalytical X'pert Phillips, Eindhoven, The Netherlands) results of the powders before and after spray drying. Scanning electron microscopy (SEM; TM3030, Hitachi Ltd, Tokyo, Japan) was performed on the spray dried spheres, before and after sintering, subsequent to grinding on SiC discs up to 1200-grit and polishing with diamond paste up to 3  $\mu\text{m}$  particle size.

### 3.4 Image Analyses

ImageJ [29] analyses were performed to determine the size distribution of the granulates from SEM images of the spray dried granulates. However, the image analyses were limited to sintered granulates because, due to their fragility, the green granulates could not be adhered to the specimen stub tape (graphite and copper). Colour thresholding was applied to distinguish the various shapes. Spherically-shaped, teardrop-shaped and peanut-shell shaped granulates were separated by outline fitting into area ranges of 0-30k, 30-60k and 60k-infinity ( $\mu\text{m}^2$ ) for

performing size distribution analysis. The SEM images were used to create a 3-dimensional polygonal mesh-based rendition of the cluster spheres using Blender [30]. 2-dimensional pictures were captured from rotating the rendition multi-axially.

## 4 Results and Discussion

### 4.1 Granulates Characteristics

Spherically shaped (SS), teardrop-shaped (TDS) and peanut-shell shaped (SS) granulates were observed in the spray dried product of S1 as shown in Figure 2. Image analysis results estimated the proportions as 61.2%, 18.4% and 20.4%, respectively.

The SS shape raises the question, *was the structure formed from incomplete break-up of a big droplet, or was the structure formed from droplets that completely atomised and then coalesced into bigger droplets?* The presence of an apex on the teardrop granulates gives a clue to the point at which the granulates in Figure 2 occurred. The teardrops can be treated as an intermediary structure between the spherically shaped and peanut-shell shaped granulates. The apex, forming at an average angle of  $112^\circ$ , suggests that the granulates were formed from the secondary atomisation of SS granulates. The relation of the apex angle analysis to the primary granulates presents an area of further study in the spray drying process. The SS, on the other hand, represent the “few large droplets at the centre of the spray pattern” [31] when external-mix pneumatic nozzles are used.



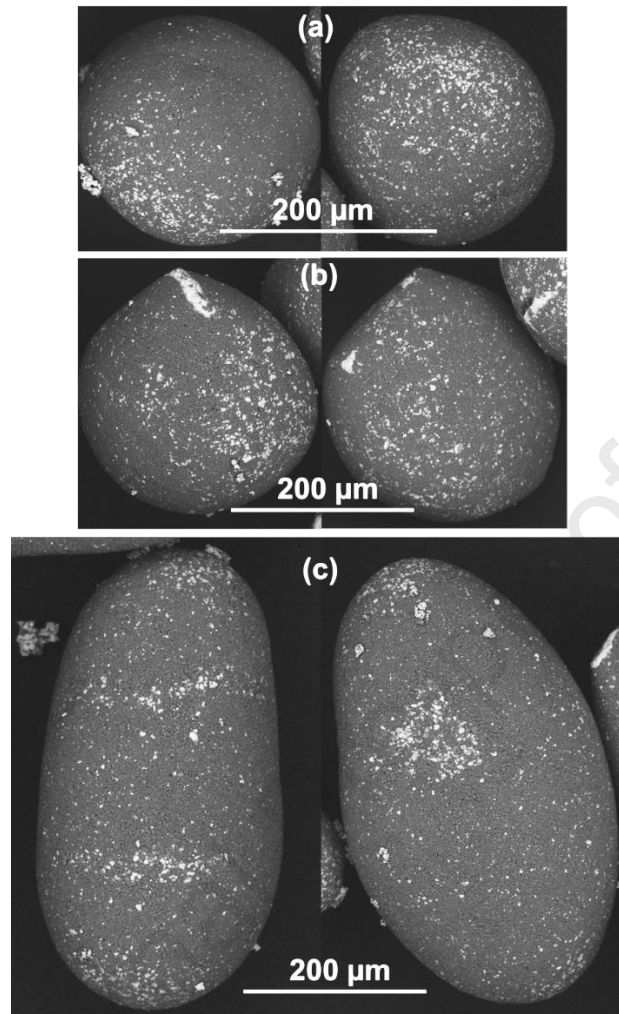


Figure 2: Morphologies of spray dried granulates obtained from the S1 slurry (a) spherically shaped, (b) teardrop-shaped, and (c) peanut-shell shaped. White speckles represent HfB<sub>2</sub> impurities.

Clustered granulates were observed (Figure 3) from the spray dried slurry S2 and not in S1. The shape consisted of multiple sub-granulates of a spherical or globular geometry. As such, the structure shall be referred to as globular cluster granulate (GCG). The 3D schematic renditions (Figure 3d) were reconstructed from multiple SEM images of the same particle. The 3D visualisation shows that the clustering behaviour of the sub-granulates was asymmetrical, giving the globular cluster granulate an irregular morphology. The schematic further confirms that the irregularity is different from the morphology of shrivelled (“wrinkled”) granulates. Clustered architectures have been demonstrated at the nanoscale in the work of Suhendi *et al.* [32],[33]. The proclivity to clustering is driven by the binder used [34]. The capillary mechanism has been used to explain the formation of agglomerates. This is discussed further in Section 3.2.

The irregularity of the globular cluster granulates may be explained by the mobility of the liquid bridges. This means the atomising gas impact can still deform the shape. Cho *et al.* [35] described a model in which the binder facilitates formation of liquid bridges between semi-

solid droplets and capillary forces help to keep the granulates together. At this stage the fluidity of the bridges mean that the shape of the cluster may be distorted. Upon evaporation of the liquid phase, an impervious shell replaces the bridges.

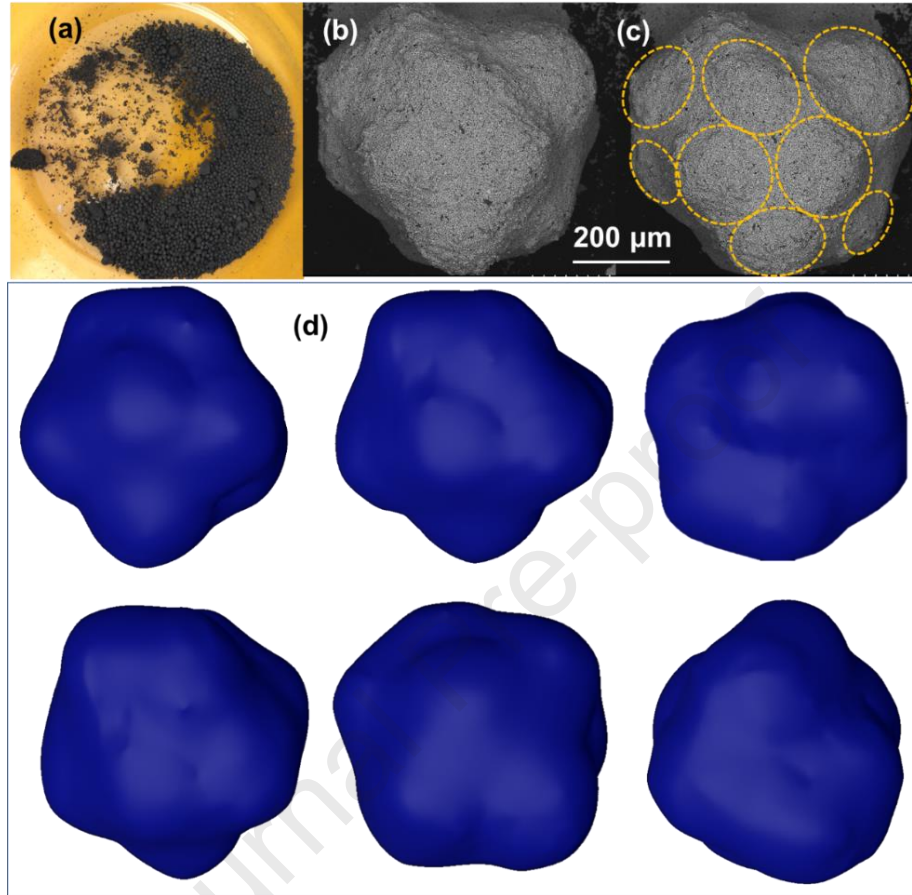


Figure 3: (a) Spray dried granulates from S2 slurry. (b) Typical granulate with a clustered morphology. (c) Granulate aggregates shown in circles. (d) 3D schematic renditions of the cluster morphology at various rotations.

Figure 4 shows the size analysis results of the granulates from Figure 2. The size analyses by the ImageJ software were based on the Feret diameter [29], which is the distance between two parallel and tangential planes bounding a granulate. The maximum and minimum Feret diameters refers to the greatest and least such distance for the granulate. The mean Feret diameters of the spherically shaped (SS), teardrop (TDS) and peanut-shell (PS) shaped granulates were  $216.4 \pm 58.7$ ,  $300.8 \pm 29.8$  and  $450.7 \pm 79.9$  μm respectively. However, the PS granulates showed a bi-modal diameter distribution; the modes were I = 420 and II = 500 μm respectively. The lower mode was observed to be for the non-necked PS (Figure 4g), while the higher mode was for the necked PS (Figure 4h). The SS showed a minimum Feret diameter of  $275.6 \pm 30.3$  μm which is comparable to the mean Feret diameter of the teardrop shape. The clustered granulates had the largest Feret diameter ( $830.0 \pm 86.4$  μm) of the granulates obtained.

The percentiles distributions presented in Figure 4 (c, f, j and m) compare the Feret diameters of the granulates which showed skewed modal histograms (Figure 4b, e and j) and a bimodal histogram (Figure 4i). 75% of the granulates were in the 150-250 μm range for SS, 230-330

$\mu\text{m}$  range for TDS and 780-920  $\mu\text{m}$  range for GCG. The linear graph confirms the validity of the Weibull analysis. The statistical geometries of the PS would link its formation to that of the SS and TDS granulates, and the occurrence of secondary atomisation. This is explained by the atomisation mechanisms involved, which can be estimated from dimensionless numbers described in the following subsection.

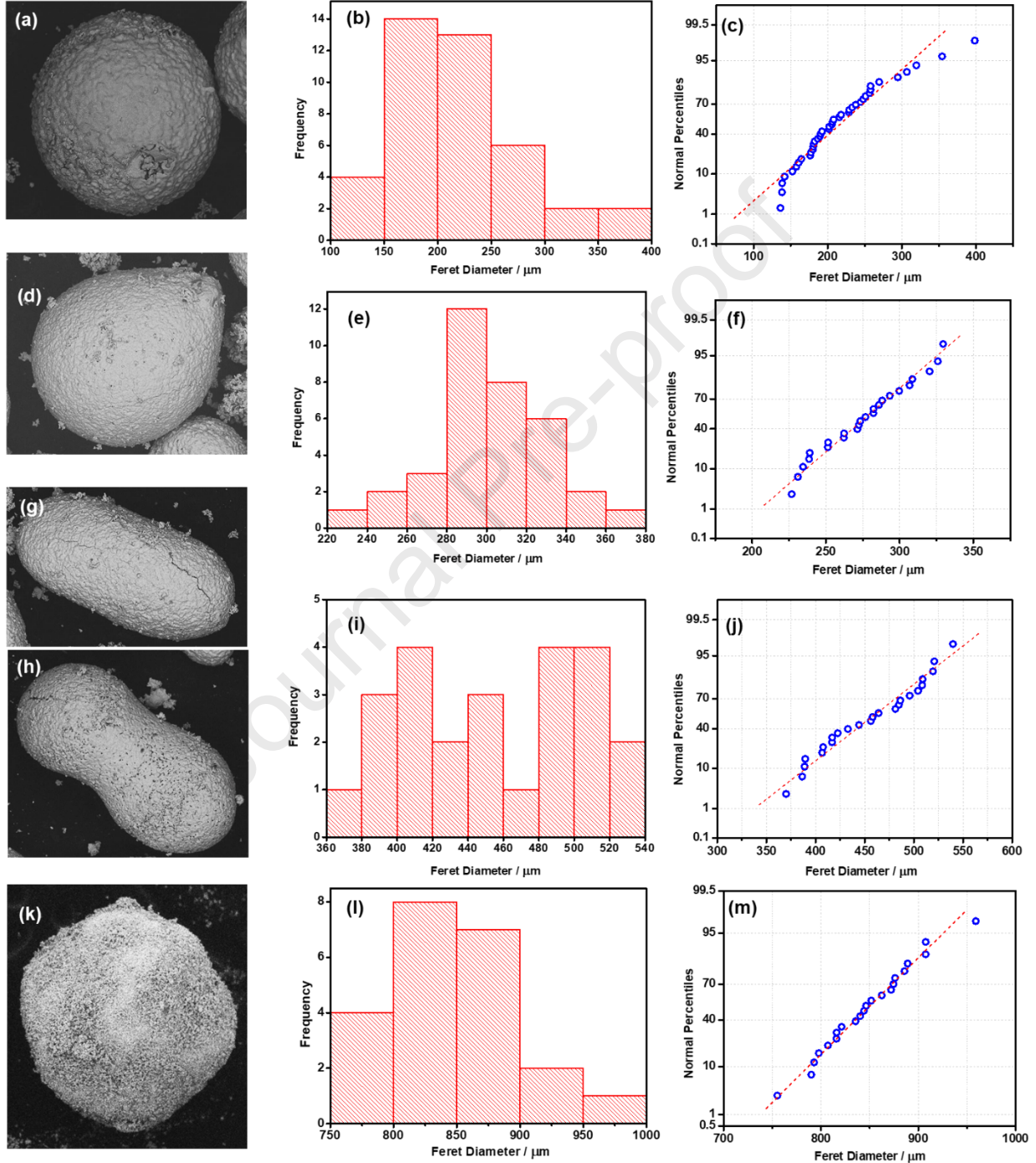


Figure 4: (a) Spherical "spherically-shaped" granulate, (d) teardrop-shaped, (g) peanut shell-shaped without distinct necking, (h) peanut shell-shaped with distinct necking, and (k) clustered granulate. The corresponding Feret diameter histograms and normal percentiles for the granulates in (a), (d), (g), (h), (k) are (b)-(c), (e)-(f), (i)-(j) and (l)-(m) respectively.

#### 4.2 Peclet, Weber and Ohnesorge Numbers Analysis

The values of the parameters used, and results of the calculations performed are presented in Table 1. It has been shown that in most systems the surface tension of water suffices [36], [37].

Table 1: Parameters and results of the atomisation dimensionless numbers.

Atomising Air		
Mass flow rate/ kg/s	3.5E-4	
Gauge pressure/ bar	5	
Exit velocity/ m/s	26	
Density / kg/m <sup>3</sup>	1204	
Slurry		
Mass flow rate/ kg/s	3.2E-3	
Droplet diameter/ m	0.0025	
Slurry exit velocity/ m/s	13	
Density/ kg/m <sup>3</sup>	4556	
Temperature/ K	298.15	
Surface tension/ N/m	72	
Shear force/ 1/s	322.5	
	Slurry 1	Slurry 2
Dynamic viscosity/ Pa·ms	26.2	35.8
Shear Stress/ N/m <sup>2</sup>	8.44	11.57
Dimensionless Numbers		
	Slurry 1	Slurry 2
Peclet number	0.16	0.21
Weber number	28.3	28.3
Ohnesorge number	0.6	1.25
Reynolds number	5.82	4.25
Gas-to-liquid ratio	0.1	0.1

The  $We$  helps to explain the physical mechanism of the slurry atomisation, which is known to transition from fluid sheets, ligaments and finally droplets as schematised in Figure 5. In this study we refer to the different  $We$  regimes described by Adiga *et al.* [38] for droplet breakup mechanisms. The obtained value of  $We = 28.3$  is within the “bag atomisation” regime which is characteristic of the range  $\sim 11 < We < \sim 35$ . In this regime large drops of slurry would be deformed by the atomising gas into a spheroid shape which transitions into a “bag” shape which eventually fragments into smaller droplets which dry into spheres. The  $Oh$  value of 0.6 and 1.25, both within the  $\sim 1$  regime, show the region in which the critical  $We$  would influence secondary atomisation in the system. At values significantly above 1 ( $Oh \gg 1$ ), the regimes would be uncertain [39].



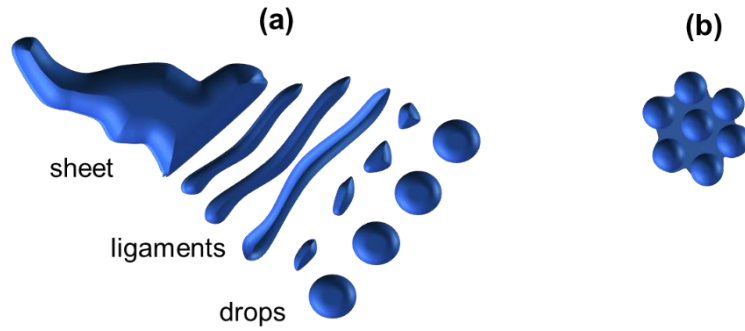


Figure 5: (a) Schematic of fluid atomisation transition regimes from sheets, to ligaments and finally droplets [39]. (b) Schematic of the capillary state of clustering in granulates. The non-spherical material represents the binder adhesion bridges across the spherical droplets [35].

#### 4.3 Sintered microspheres: Internal Dual Structures

A core-shell microstructure was observed in the slurry S1 granulates, particularly the TDS and PS as shown in Figure 6(a) and (b,c), respectively. The core consisted of a three-dimensional architecture of interconnected globular agglomerates with void channels. This core-shell microstructure is of similar resemblance to that obtained by Walton and Mumford [24] after spray drying tri-sodium orthophosphate at an inlet temperature of 400 °C.

The shell thickness was estimated as 8-12  $\mu\text{m}$  in the sections measured by SEM analysis (shown in Figure 6(d)). The sections labelled P and Q Figure 6(e) reveal a migration of the shell structure into the core, suggesting the partial infiltration of liquid phase into the peripheral voids. The grain structure of the shell showed a well sintered network of equiaxed grains estimated at 22  $\mu\text{m}$  size by ImageJ analysis of SEM images. Cracking was observed in the SS shell, mostly at the lobes and running across the shape (shown in Figure 6(b)), having been exacerbated by ceramographic preparation (mounting, grinding and polishing).

Cho *et al.* [35] explained how the morphology forms in clustered granulates, drawing on the classical Newitt and Conway-Jones theory in which at the capillary stage of agglomeration, liquid bridges form between solid particles promoting adhesion and granulate strength. Similarly, the clumping in the globular cluster shape granulate arises from capillary forces at the liquid bridges that form in the system during atomisation. The surface tension in the liquid contributes to capillary adhesion which pulls the solid particles inward, and the liquid surface forms a self-supporting shell. The PEG binder increases the surface tension of the particle interfaces and promotes adhesion [35].

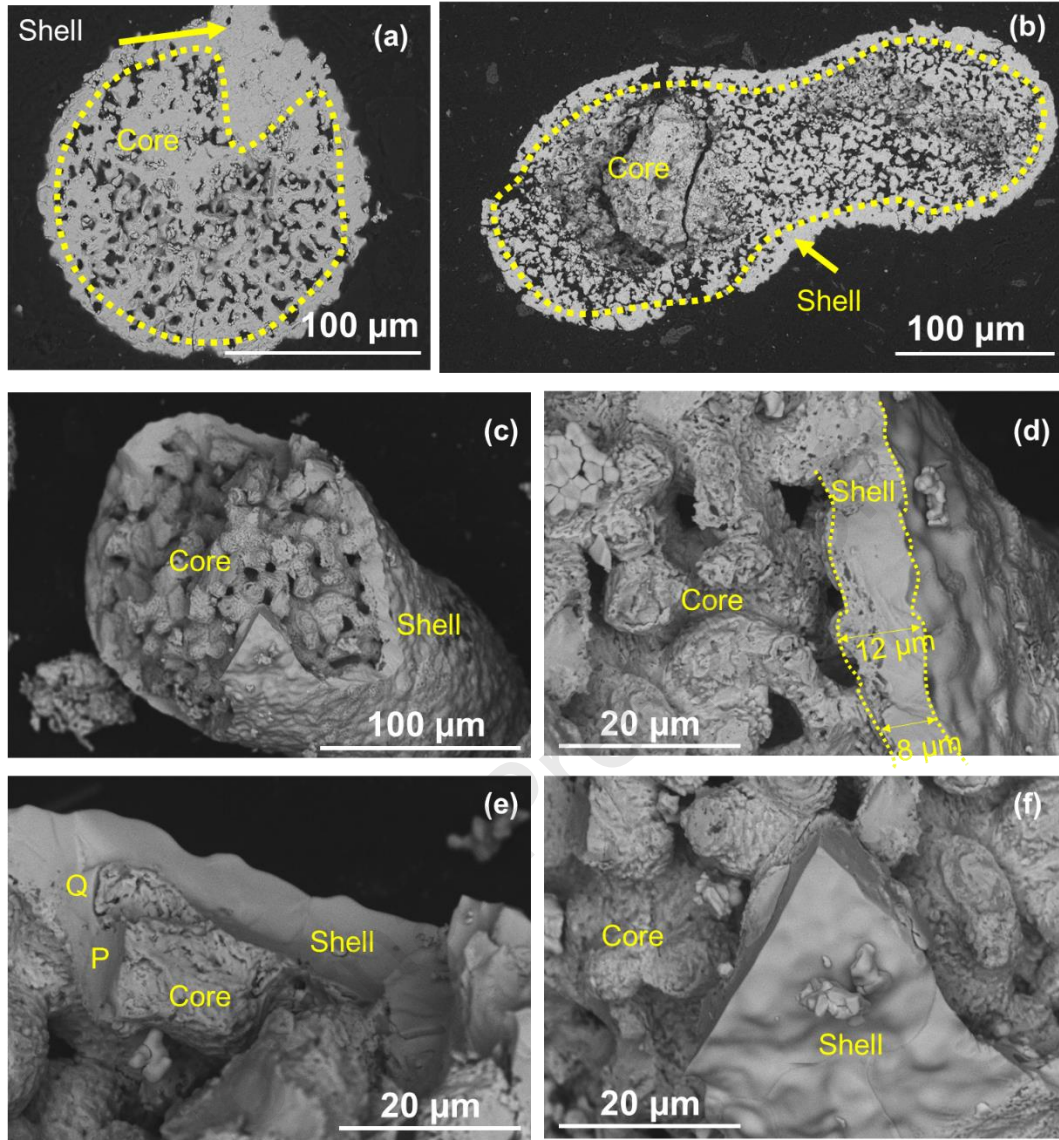


Figure 6: SEM images of  $\text{ZrB}_2$  granulates post-sintering. (a) Cross-section of a teardrop granulate. (b) Cross-section of a peanut shell shaped. (c)-(f) Microstructures of the core-shell structure of a fractured peanut shell shaped granulate.

#### 4.4 Sintered microspheres: External Dual Structures

Figure 7 shows the cross-section of the globular cluster granulate (GCG). The core-shell structure was not observed in the GCG as shown in Figure 7(c), (e)-(f). On the contrary, a denser microstructure was observed on the inside of the granulate than outside Figure 7(b). This suggests that the impact of the discrete granulate during self-assembly was perfect. Additionally, the discrete granulates were entirely solid before self-assembly.

The bridges that are formed by the action of the binder can have an overall effect of engulfing bridges (leading to internal structures) or interconnecting (leading to external clusters). The difference is attributable to the viscosity action (influenced by the binder quantity used). Subsequently, the action of the fluid flow differences described by the Peclet and Ohnesorge

numbers, confirm the link between binder effect on viscosity and the mechanism of bridge motions during atomisation.

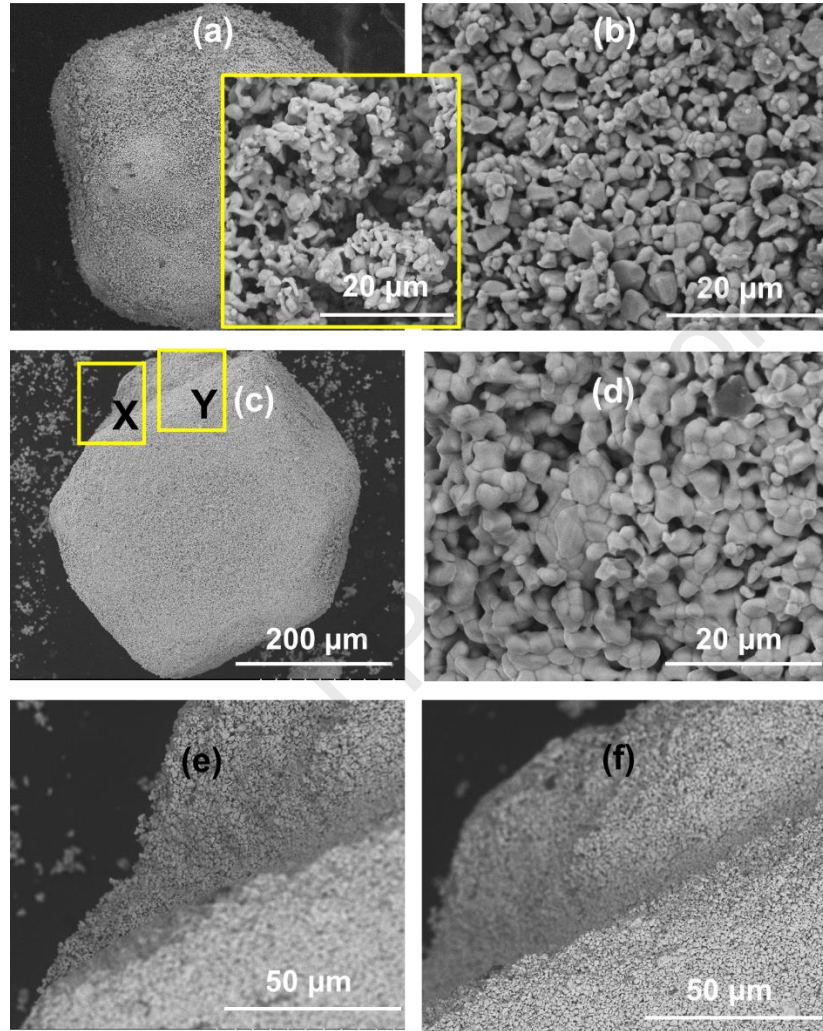


Figure 7: SEM images of clustered  $\text{ZrB}_2$  granulate. (a) After sintering. (b) Microstructure of surface and of loose particles on surface in insert. (c) Cross-sectioned clustered  $\text{ZrB}_2$  sphere post-sintering and internal microstructure in (d). (e) Microstructure showing absence of a shell structure at the clustered sphere edge labelled X in (c) and (f) for the edge labelled Y in (c).

The architectures of both the core-shell and clustered granulates provide opportunities for the dual-scale composite architecture (DCA) concept [40] for composite fuels. The containment of sub-granulates of micro- and meso-scale in the overall granulates demonstrates the dual architecture. We predict that this architecture will enable the accommodation of nuclear fission products and property variations that is expected during water reactor operation. The effect of such architectures when dispersed in a uranium dioxide matrix deserves further investigation.

#### 4.5 Oxidation Resistance During Spray Drying

It was important to evaluate the oxidation propensity of the  $\text{ZrB}_2$  powders during spray drying at the inlet air set point of 250 °C and an actual maximum recorded temperature of 221 °C. The



XRD patterns obtained pre- and post-spraying are shown in Figure 8. The peaks for both patterns were matched to the  $\text{ZrB}_2$  (PDF 96-151-0857) phase. No traces of oxygen were detected by this method of characterization, suggesting that  $\text{ZrB}_2$  was oxidation resistant at the spray drying temperatures used. The oxidation stability of  $\text{ZrB}_2$  is dependent on the temperature and oxygen partial pressure in the system [10], [11] and an oxidation onset temperature of  $\sim 690^\circ\text{C}$  have been reported [41]. The systematic shift in the  $\text{ZrB}_2$  peaks in both the as-received powder and spray dried granulates is attributed to  $\text{HfB}_2$  impurities which may exist in the  $\text{ZrB}_2$  lattice volume.

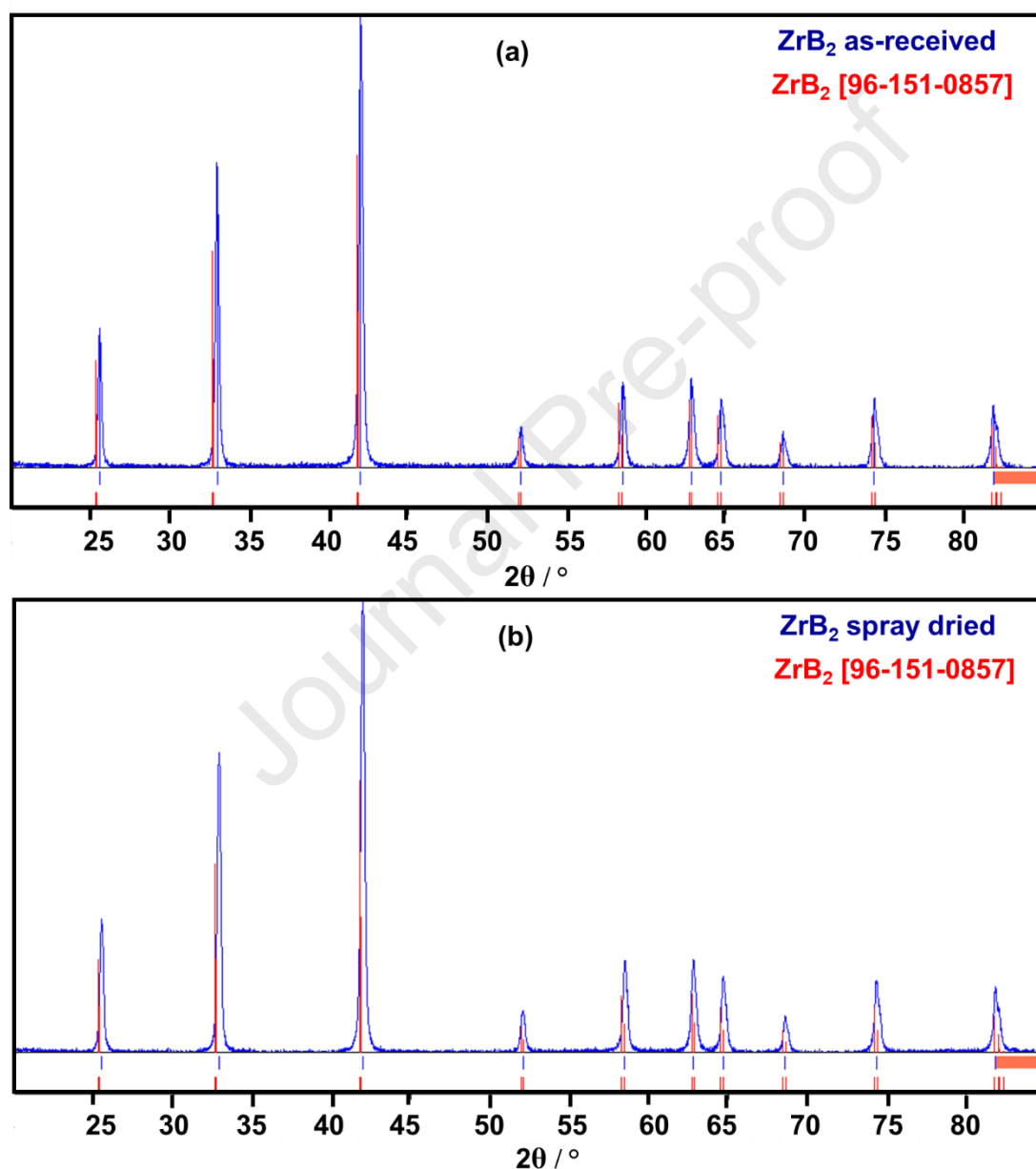


Figure 8: XRD spectra for the  $\text{ZrB}_2$  powder (a) before spray drying, and (b) after spray drying.

## 5 Summary and Conclusions

Self-contained dual-scale composite architectures (DCA) were obtained in spray dried and sintered zirconium diboride microspheres. Three-dimensional architectures of internally and externally detailed sub-microspheres of micro- and meso-scales in the overall microspheres demonstrated the dual composite architectures.

1. The architecture of the granulates depend on the binder used; 2 wt% leads to spherical and related variations of granulates, while 4 wt% leads to clustering of spherical granulates.
2. Spherical granulates of  $216.4 \pm 58.7 \mu\text{m}$  diameter were obtained as well as related structures of teardrop ( $300.8 \pm 29.8 \mu\text{m}$  Feret diameter) and peanut-shell shapes ( $450.7 \pm 79.9 \mu\text{m}$  Feret diameter) for binder of 2 wt% of the zirconium diboride powder used.
3. The globular clustered granulates had the largest Feret diameter ( $830.0 \pm 86.4 \mu\text{m}$ ) of the granulates obtained for binder of 4 wt% of the zirconium diboride powder used.
4. Calculated dimensionless Peclet, Weber and Ohnesorge numbers of 0.16-0.21, 28.3, and 0.6-1.3 were obtained respectively and related to the morphologies of the microspheres obtained. Peclet numbers below 1 signify favourable conditions for solid microspheres.
5. Spray drying of zirconium diboride can be performed in air at  $250^\circ\text{C}$  without oxidation being evident in X-ray diffraction.

The materials produced have potential as nuclear fuel additives where this architecture may enable efficient accommodation of fission products and property changes expected during reactor operation.

## 6 Declaration of Competing Interest

The authors declare that they have no known competing financial interests or personal relationships that could have appeared to influence the work reported in this paper.

## 7 Acknowledgements

This research was funded under the £46m Advanced Fuel Cycle Programme as part of the Department for Business, Energy and Industrial Strategy's (BEIS) £505m Energy Innovation Programme. SCM was funded through the Sêr Cymru II programme by Welsh European Funding Office (WEFO) under the European Development Fund (ERDF).

## 8 References

- [1] J. Gulliford, "Overview of Current Understanding of Accident Progression at Fukushima Dai-ichi," 2012.
- [2] K. A. Terrani, L. L. Snead, and J. C. Gehin, "Microencapsulated fuel technology for

- commercial light water and advanced reactor application,” *J. Nucl. Mater.*, vol. 427, no. 1–3, pp. 209–224, 2012, doi: 10.1016/j.jnucmat.2012.05.021.
- [3] J. Turner, F. Martini, J. Buckley, G. Phillips, S. C. Middleburgh, and T. J. Abram, “Synthesis of candidate advanced technology fuel: Uranium diboride (UB<sub>2</sub>) via carbo/borothermic reduction of UO<sub>2</sub>,” *J. Nucl. Mater.*, vol. 540, p. 152388, 2020, doi: 10.1016/j.jnucmat.2020.152388.
- [4] B. Gong *et al.*, “U<sub>3</sub>Si<sub>2</sub> and UO<sub>2</sub> composites densified by spark plasma sintering for accident-tolerant fuels,” *J. Nucl. Mater.*, vol. 534, 2020, doi: 10.1016/j.jnucmat.2020.152147.
- [5] J. H. Yang, D. J. Kim, K. S. Kim, and Y. H. Koo, “UO<sub>2</sub>-UN composites with enhanced uranium density and thermal conductivity,” *J. Nucl. Mater.*, vol. 465, pp. 509–515, 2015, doi: 10.1016/j.jnucmat.2015.06.039.
- [6] B. J. Jaques *et al.*, “Synthesis and sintering of UN-UO<sub>2</sub> fuel composites,” *J. Nucl. Mater.*, vol. 466, pp. 745–754, 2015, doi: 10.1016/j.jnucmat.2015.06.029.
- [7] J. M. Lonergan, W. G. Fahrenholtz, and G. E. Hilmas, “Zirconium diboride with high thermal conductivity,” *J. Am. Ceram. Soc.*, vol. 97, no. 6, pp. 1689–1691, 2014, doi: 10.1111/jace.12950.
- [8] J. K. Fink, “Thermophysical properties of uranium dioxide,” *Nucl. Mater.*, vol. 102, no. 1–2, pp. 17–25, 2000.
- [9] W. G. Fahrenholtz, E. J. Wuchina, W. E. Lee, and Y. Zhou, “Introduction,” in *Ultra-High Temperature Ceramics: Materials for Extreme Environment Applications*, W. L. and Y. Z. (Editors) WG Fahrenholtz, EJ Wuchina, Ed. Wiley, 2014, pp. 1–5.
- [10] E. Wuchina, E. Opila, M. Opeka, W. Fahrenholtz, and I. Talmy, “UHTCs - Ultra-High Temperature Ceramic Materials for Extreme Environment Applications,” *Electrochem. Soc. Interface*, vol. 16, no. 4, pp. 30–36, 2007.
- [11] L. Kaufman and E. Clougherty, “Investigation of boride compounds for very high temperature applications, Part I. No. TRD-TDR-63-4096-PT-1,” Cambridge MA, 1963.
- [12] E. W. Neuman, G. E. Hilmas, and W. G. Fahrenholtz, “Strength of Zirconium Diboride to 2300 °C,” *J. Am. Ceram. Soc.*, vol. 96, no. 1, pp. 47–50, 2013, doi: 10.1111/jace.12114.
- [13] L. Silvestroni, H. J. Kleebe, W. G. Fahrenholtz, and J. Watts, “Super-strong materials for temperatures exceeding 2000°C,” *Sci. Rep.*, vol. 7, no. January, pp. 1–8, 2017, doi: 10.1038/srep40730.
- [14] A. D. Angio, J. Zou, J. Binner, H. Ma, G. E. Hilmas, and W. G. Fahrenholtz, “Journal of the European Ceramic Society Mechanical properties and grain orientation evolution of zirconium diboride-zirconium carbide ceramics,” *J. Eur. Ceram. Soc.*, vol. 38, no. 2, pp. 391–402, 2018, doi: 10.1016/j.jeurceramsoc.2017.09.013.
- [15] E. C. Auden *et al.*, “Thermal neutron-induced single-event upsets in microcontrollers containing boron-10,” *IEEE Trans. Nucl. Sci.*, vol. 67, no. 1, pp. 29–37, 2020.

- [16] W. Chubb, "Coating a uranium dioxide nuclear fuel with a zirconium diboride burnable poison. U.S. Patent 4,582,676.," 1986.
- [17] Westinghouse Electric Company, "Nuclear Fuel: Integral Fuel Burnable Absorber (IFBA) fuel cycles and IFBA/Gad hybrid fuel cycles. Report NFCM-0015.," 2018.
- [18] L. M. Garrison, G. L. Kulcinski, G. Hilmas, W. Fahrenholtz, and H. M. Meyer, "The response of ZrB<sub>2</sub> to simulated plasma-facing material conditions of He irradiation at high temperature," *J. Nucl. Mater.*, vol. 507, pp. 112–125, 2018, doi: 10.1016/j.jnucmat.2018.04.016.
- [19] B. G. Charlton and P. G. Alfredson, "Preliminary design and cost considerations for a plant to produce nuclear purity uranium dioxide from Australian ore concentrates," 1971.
- [20] D. M. Levins, P. G. Alfredson, R. C. Hirst, and P. R. Macbride, "Spray drying of ammonium diuranate slurries, AAEC/E226," 1972.
- [21] R. Vehring, W. R. Foss, and D. Lechuga-Ballesteros, "Particle formation in spray drying," *J. Aerosol Sci.*, vol. 38, no. 7, pp. 728–746, 2007, doi: 10.1016/j.jaerosci.2007.04.005.
- [22] R. Vehring, "Pharmaceutical particle engineering via spray drying," *Pharm. Res.*, vol. 25, no. 5, pp. 999–1022, 2008, doi: 10.1007/s11095-007-9475-1.
- [23] E. Guyon, J. P. Hulin, L. Petit, and P. G. de Gennes, *Guyon, E., Hulin, J. P., Petit, L., & de Gennes, P. G. (2001). Hydrodynamique physique*, 3rd ed. Les Ulis, France: EDP Sciences, 2012.
- [24] D. E. Walton and C. J. Mumford, "The morphology of spray-dried particles. The effect of process variables upon the morphology of spray-dried particles," *Chem. Eng. Res. Des.*, vol. 77, no. 5, pp. 442–460, 1999, doi: 10.1205/026387699526296.
- [25] J. D. Kaser, "Evaluation of Atomizing Nozzles for the Spray Solidification of Radioactive Waste, BNWL-I066," Richland, Washington, 1969.
- [26] P. Walzel, "Influence of the spray method on product quality and morphology in spray drying," *Chem. Eng. Technol.*, vol. 34, no. 7, pp. 1039–1048, 2011, doi: 10.1002/ceat.201100051.
- [27] S. P. Rao, S. S. Tripathy, and A. M. Raichur, "Dispersion studies of sub-micron zirconia using Dolapix CE 64," *Colloids Surfaces A Physicochem. Eng. Asp.*, vol. 302, no. 1–3, pp. 553–558, 2007, doi: 10.1016/j.colsurfa.2007.03.034.
- [28] Yamato Scientific, "Instruction manual spray dryer," *Yamato Sci. Am. Inc.*, pp. 1–12, 2012.
- [29] K. W. Schneider, C. A., Rasband, W. S., & Eliceiri, "NIH Image to ImageJ: 25 years of image analysis," *Nat. Methods*, vol. 9, no. 7, pp. 671–675, 2012.
- [30] Blender Foundation, "Blender version 2.92," 2021. <http://www.download.blender.org>. (accessed Apr. 27, 2021).

- [31] M. A. Miller and L. A. Stout, "Design and performance of atomizing nozzles for spray calcination of high-level wastes, PNL-3702," 1981.
- [32] A. B. D. Nandiyanto, A. Suhendi, O. Arutanti, T. Ogi, and K. Okuyama, "Influences of surface charge, size, and concentration of colloidal nanoparticles on fabrication of self-organized porous silica in film and particle forms," *Langmuir*, vol. 29, no. 21, pp. 6262–6270, 2013, doi: 10.1021/la401094u.
- [33] A. Suhendi, A. B. D. Nandiyanto, M. M. Munir, T. Ogi, L. Gradon, and K. Okuyama, "Self-assembly of colloidal nanoparticles inside charged droplets during spray-drying in the fabrication of nanostructured particles," *Langmuir*, vol. 29, no. 43, pp. 13152–13161, 2013, doi: 10.1021/la403127e.
- [34] T. Schæfer, "Growth mechanisms in melt agglomeration in high shear mixers," *Powder Technol.*, vol. 117, no. 1–2, pp. 68–82, 2001, doi: 10.1016/S0032-5910(01)00315-1.
- [35] S. Y. Cho, F. Takahashi, and F. L. Dryer, "Some Theoretical Considerations on the Combustion and Disruption of Free Slurry Droplets," *Combust. Sci. Technol.*, vol. 67, no. 1–3, pp. 37–57, 1989, doi: 10.1080/00102208908924060.
- [36] S. Poozesh, S. W. Grib, M. W. Renfro, and P. J. Marsac, "Near-field dynamics of high-speed spray dryer coannular two fluid nozzle: Effects of operational conditions and formulations," *Powder Technol.*, vol. 333, pp. 439–448, 2018, doi: 10.1016/j.powtec.2018.04.064.
- [37] S. Mandato *et al.*, "Liquids' atomization with two different nozzles: Modeling of the effects of some processing and formulation conditions by dimensional analysis," *Powder Technol.*, vol. 224, pp. 323–330, 2012, doi: 10.1016/j.powtec.2012.03.014.
- [38] K. C. Adiga, H. D. Willauer, R. Ananth, and F. W. Williams, "Implications of droplet breakup and formation of ultra fine mist in blast mitigation," *Fire Saf. J.*, vol. 44, no. 3, pp. 363–369, 2009, doi: 10.1016/j.firesaf.2008.08.003.
- [39] N. Dombrowski and W. R. Johns, "The aerodynamic instability and disintegration of viscous liquid sheets," *Chem. Eng. Sci.*, vol. 18, no. 7, p. 470, 1963, doi: 10.1016/0009-2509(63)80037-8.
- [40] M. P. Harmer, H. M. Chan, and G. A. Miller, "Unique Opportunities for Microstructural Engineering with Duplex and Laminar Ceramic Composites," *J. Am. Ceram. Soc.*, vol. 75, no. 7, pp. 1715–1728, 1992.
- [41] R. Hassan and K. Balani, "Oxidation kinetics of ZrB<sub>2</sub>- and HfB<sub>2</sub>-powders and their SiC reinforced composites," vol. 177, no. May, 2020, doi: 10.1016/j.corsci.2020.109024.

**Declaration of interests**

*Article:* **Self-contained dual-scale composite architectures in spray dried zirconium diboride**

☒ The authors declare that they have no known competing financial interests or personal relationships that could have appeared to influence the work reported in this paper.

☐ The authors declare the following financial interests/personal relationships which may be considered as potential competing interests: